Published in final edited form as:
*Nanomedicine*. 2011 February ; 7(1): 97–106. doi:10.1016/j.nano.2010.09.003.

# Enhanced Optical Breakdown in KB Cells Labeled with Folate-Targeted Silver/Dendrimer Composite Nanodevices

**Christine Tse, Ph.D.**[1,*], **Marwa J. Zohdy, Ph.D.**[1], **Jing Yong Ye, Ph.D.**[2,3], **Matthew O'Donnell, Ph.D.**[1,4], **Wojciech Lesniak, Ph.D**[5], and **Lajos Balogh, Ph.D.**[5]

[1]University of Michigan, Department of Biomedical Engineering, Ann Arbor, MI 48109

[2]University of Michigan, Center for Ultrafast Optical Science, Ann Arbor, MI 48109

[3]University of Texas at San Antonio, Department of Biomedical Engineering, San Antonio, TX 78249

[4]University of Washington, Bioengineering Department, Seattle, WA 98195

[5]Roswell Park Cancer Institute, Department of Radiation Medicine, Buffalo, NY 14263

## Abstract

Enhanced optical breakdown of KB cells (a human oral epidermoid cancer cell known to overexpress folate receptors) targeted with silver/dendrimer composite nanodevices (CNDs) is described. CNDs $\{(Ag^0\}_{25}$-PAMAM_E5.$(NH_2)_{42}(NGly)_{74}(NFA)_{2.7}\}$ were fabricated by reactive encapsulation, using a biocompatible template of dendrimer-folic acid (FA) conjugates. Preferential uptake of the folate-targeted CNDs (of various treatment concentrations and surface functionality) by KB cells was visualized with confocal microscopy and transmission electron microscopy (TEM). Intracellular laser-induced optical breakdown (LIOB) threshold and dynamics were detected and characterized by high-frequency ultrasonic monitoring of resulting transient bubble events. When irradiated with a near-infrared (NIR), femtosecond laser, the CND-targeted KB cells acted as well-confined activators of laser energy, enhancing nonlinear energy absorption, exhibiting a significant reduction in breakdown threshold, and thus selectively promoting intracellular LIOB.

### Keywords

dendrimer; nanocomposite; folate targeting; laser enhanced breakdown; acoustic characterization; microbubbles; cancer; photomechanical therapy



* Corresponding Author: Address: Department of Biomedical Engineering, University of Michigan, Ann Arbor, Michigan, USA; ctse@umich.edu.



**SUPPORTING INFORMATION**

The contents of Supporting Information includes experimental procedures, figures, and supplemental material relating to 1) Folate-Functionalized PAMAM Dendrimer Template Preparation and Characterization, 2) Folate-Targeted Silver CND Preparation and Characterization, 3) KB Cell Incubation with CNDs, 4) Imaging Cellular Uptake of CNDs, and 5) the Laser Irradiation and High Frequency Acoustic Monitoring System.

## BACKGROUND

Nanoparticles with unique and tunable optical properties may enable novel cellular therapy methods [1-14]. Several investigations have biologically targeted metal nanoparticles to efficiently convert linearly absorbed laser energy into localized heat for selective photothermal cancer therapy [6-8,10,12,14]. Multifunctional nanoparticles targeted to specific receptors on cancerous cells selectively enhance energy absorption and decrease the laser dose required to generate thermal damage in the targeted regions [1,3,6]. The selectivity of this linear optical absorption based technique depends on the efficacy of nanoparticle targeting strategies, the minimization of thermal diffusion (via irradiation time and pulse duration), and the nanoparticle absorption characteristic within the optimal biological transmittance NIR spectral band. Researchers have investigated NIR tunable nanostructures including nanoshells [1,3,5], nanorods [11], and nanoclusters [5,7,13] for photothermal applications.

Nanoparticle-mediated applications based on the nonlinear effects of NIR, ultrashort-pulsed LIOB, however, have been largely unexplored. LIOB is a plasma-mediated ablation process based on nonlinear energy absorption, where photomechanical breakdown occurs only in regions exposed to laser intensities exceeding a material-specific threshold. In traditional geometrical targeting, laser beam focusing is used to shape the local laser intensity, defining a spatially restricted breakdown region at the focus and minimizing effects to surrounding material due to limited heat diffusion time [15]. Utilizing this geometrical targeting scheme, NIR, femtosecond LIOB has already been demonstrated to produce highly precise cell effects [16-20]. This paper presents an alternative nonlinear breakdown scheme, however, by using the presence and concentration of metal/dendrimer CNDs targeted to cells to define the spatial distribution of the breakdown threshold and thus the breakdown region. Figure 1 illustrates the contrasting principles involved in biochemical versus geometrical targeting breakdown schemes.

Metal/dendrimer CNDs are water-soluble, biocompatible, and stable inorganic/organic hybrids synthesized by topologically trapping very small metallic domains in nanoscopic size polymeric networks (i.e., PAMAM dendrimers) using reactive encapsulation [21-23]. Due to the molecular level mixing of the organic and inorganic components, metal CNDs exhibit unique properties. Previous studies from our group have demonstrated that metal/dendrimer nanocomposites (with absorption peaks in the ultraviolet (UV) region) enhance the nonlinear absorption of NIR light, greatly reducing the femtosecond LIOB threshold in aqueous solutions, and leading to breakdown at energy levels two magnitudes lower than those of any organic material (i.e., live cells) [24-25]. In other words, laser power levels for photodisruption of the CNDs would be harmless for unlabeled organic material.

Furthermore, because metal CNDs still interact with their environment primarily through the surface of their dendrimer host, biochemical molecular targeting is possible through surface engineering [26]. Targeting (e.g., to tumor cells) is flexible and can be either to cell or tissue receptors. Various targeting groups including organic molecules, antibodies and peptides can be covalently attached to a dendrimer surface [27-30]. Specifically, dendrimer-based folate contrast agents targeting tumors and tumor cells have also been developed [31]. Coupling folate to dendrimers targets them to endogenous folate binding proteins that exist in both the serum of patients with cancer and on the cell surface of many human cancers of epithelial origin. This principle (i.e., PAMAM dendrimers with FA at the periphery) has been demonstrated by Wiener et al. in a series of papers between 1997 and 2003 [31,32]. Fluorescence studies have shown that KB tumor cells (found in human squamous cell carcinomas) expressing the high-affinity folate receptor accumulated a fluorescent dendrimer-folate conjugate in a receptor specific manner. In addition, the same studies

showed that after rapid and specific binding, folate targeted PAMAM dendrimers were internalized by tumor cells [32]. Consequently we selected this system to test whether threshold reduction exists in a biological system, and to demonstrate the applicability of selective breakdown mediated by targeted CNDs.

Fabrication and characterization results are described, investigating $\{(Ag^0\}_{25}$-PAMAM_E5.$(NH_2)_{42}(NGly)_{74}(NFA)_{2.7}\}$, a FA conjugated, amino-hydroxyl-terminated silver/dendrimer nanodevice (FA- $\{Ag^0\}$, for short), designed to target KB tumor cells through the folate receptor. Silver CNDs are fluorescent when excited at UV wavelengths of 300-400 nm, so targeted cellular uptake of the folate-conjugated CND construct could be visualized with confocal microscopy [33]. Lesniak, et al. have recently demonstrated *in vitro* that although amine terminated silver CNDs are toxic at 1μM concentration, hydroxyl-terminated silver-CNDs exhibit minimal nonspecific uptake and are nontoxic at concentrations of up to 2μM. Therefore, in this study, 2/3rd of the primary amine termini (that are positively charged at pH 7.4) were reacted with glycidol ($CH_2OCHCH_2OH$) to reduce charge-related toxicity, and concentrations used were less than 2μM to test specific uptake through folate targeting.

Both folate-targeted and non-targeted CNDs were used to investigate differences in cellular uptake and nanodevice-loading of cells, to test the selective reduction of LIOB threshold in targeted KB cells, and to monitor the production of mechanical intracellular laser effects, including microbubble formation and collapse. Intracellular, laser-induced bubbles provided high acoustic contrast for acoustically monitored breakdown studies in cell cultures. High frequency ultrasound monitors generation, fate, and collapse of microbubbles and could characterize LIOB by detecting its mechanical effects, including acoustic radiation and pulse-echo signals from resulting microbubbles. Successive recordings displayed in a wavefield form provided an “image” of breakdown dynamics [20,25,34].

Summarily, we describe the synthesis and characterization of a new folate-targeted silver/dendrimer CND, study *in vitro* binding to KB cells overexpressing the folate receptor, and study the potential of this silver CND to enhance intracellular breakdown in labeled KB cells. Understanding aspects of CND enhanced intracellular breakdown and determining desirable targeting conditions for breakdown enhancement are both important to applying a CND-mediated LIOB scheme to potential laser diagnostic and therapy methods at the level of single cells.

## METHODS

### Silver CND Fabrication

We previously demonstrated fabrication of amino, glycidol, and succinamic acid terminated silver/dendrimer nanodevices and their application as fluorescent cell labels [33]. As an extension of these studies, we prepared FA targeted silver CND for specific targeting of KB cells, overexpressing folate receptors, and enhanced intracellular femtosecond LIOB threshold, since we have previously shown that the presence of metal/dendrimer nanodevices greatly influence this phenomenon in aqueous solution [24-25].

In the first step the PAMAM_E5.$(NH_2)_{119}$ dendrimer was partially glycidolated, followed by conjugation with FA as shown in Figure 2A. Starting material and synthetic products were purified and characterized by means of polyacrylamide gel electrophoresis (PAGE), size exclusion chromatography (SEC), potentiometric titration, matrix assisted laser desorption ionization - time of flight mass spectrometry (MALDI-TOF), and nuclear magnetic resonance (NMR). SEC was used to determine the average molecular masses of the dendrimers and dendrimer derivatives (E5.$(NH_2)_{119}$ (starting material), E5.$(NH_2)_{45}(NGly)_{74}$ (intermediate) product, and E5.$(NH_2)_{42}(NGly)_{74}(NFA)_{2.7}$). Measurements

were performed using an Alliance Waters 2690 separation module equipped with an ultraviolet-visible (UV-vis) detector (Waters Corp, Milford MA, USA), a Wyatt Dawn laser (690 nm) photometer and an Optilab interferometric refractometer, operating at 685 nm (Wyatt Technology Corporation, Santa Barbara, CA, USA). Phosphate buffer (0.05 M, pH 2.5) with 0.025% sodium azide was used as the mobile phase. The flow rate was maintained at 0.6 mL/min. For separation, three Waters columns were used: Ultrahydrogel 500 (7.8x300mm), Ultrahydrogel 250 (7.8×300mm) and Ultrahydrogel 120 (7.8×300mm). Sample concentration was kept at 2 mg/mL and 100 μL was injected. Data were elaborated using Astra, Empower and PeakFit software packages (Wyatt Technology Corporation, Santa Barbara, CA, USA; Waters Corp, Milford, MA, USA and Systat Software San Jose, CA, USA).

This PAMAM_E5.$(NH_2)_{42}(NGly)_{74}(NFA)_{2.7}$ dendrimer template was used to fabricate silver/dendrimer composite nanoparticles. Briefly, the [$(Ag^+)_{25}$-PAMAM_E5.$(NH_2)_{42}(NGly)_{74}(NFA)_{2.7}$] silver-dendrimer complex was obtained by mixing aqueous solutions of dendrimer templates at pH 2.5 and $AgNO_3$ at a 1:25 molar ratio at room temperature. The pH was slowly increased to pH=7.4 by titrating the complex with 0.1 M NaOH solution (final dendrimer concentration of 2 mg/mL) while stirring. The colorless solution of silver-dendrimer complex was irradiated with a UV lamp for 12 hours to reduce the $Ag^+$ ions photochemically. The resulting composite nanoparticles {$(Ag^0)_{25}$-PAMAM_E5.$(NH_2)_{42}(NGly)_{74}(NFA)_{2.7}$}, (FA-{$Ag^0$} for short) were characterized by polyacrylamide gel electrophoresis (PAGE), UV-vis, and fluorescence spectroscopy, dynamic light scattering, zeta potential measurements, and TEM. Detailed preparation and characterization of {$(Ag^0)_{25}$-PAMAM_E5.$(NGly)_{119}$} CND, which was used as a control in biological studies, has been already described in our previous report [33].

## Cell Incubations

Cell treatment conditions included a negative control (no CND incubation), 2) incubation with 0.05 μM targeted CND (FA-{$Ag^0$}) solution, 3) incubation with 0.5 μM targeted CND solution, 4) incubation with 0.5 μM untargeted {$Ag^0$} (without FA), and 5) incubation with 0.5 μM targeted dendrimer template PAMAM_E5.$(NH_2)_{42}(NGly)_{74}(NFA)_{2.7}$ (i.e., without silver). Cells were incubated for twenty-four hours for all conditions.

CND incubation concentration was chosen based on our previous report [33] indicating that {$(Ag^0)_{25}$-PAMAM_E5.NGly} nanodevices with the same terminal functionalities and surface charge similar to {$(Ag^0)_{25}$-PAMAM_E5.$(NH_2)_{42}(NGly)_{74}(NFA)_{2.7}$} are not toxic to KB cells within a concentration range of 0-2 μM. FA itself is a well known vitamin regularly given to pregnant women. Presence of an average of 2.7 FA residues per dendrimer template will not influence their overall toxicity profile, as folated dendrimer nanodevices have also been reported with minimal or no toxicity.

## Confocal Imaging

Utilizing the fluorescence of silver CNDs [33], confocal microscopy was used to visualize the uptake of folate-targeted silver CNDs by KB cells. To calibrate fluorescence images, silica beads (d=5 μm) precoated by the same CND used in the experiment were added to cell dishes prior to imaging and used as fluorescence intensity standards. These calibration beads appear alongside cells in all images as regular spheres. Cell and calibration bead boundaries in fluorescence images were verified with corresponding brightfield images. Fluorescence images shown are single, 7.5 μm optical sections corresponding to focal planes approximating the middle of imaged cells. For all fluorescence images, gain and offset settings were adjusted to give the strongest cell fluorescence intensity while still avoiding pixel saturation.

Images were analyzed using the NIH Image J software (Office of Research Services, Bethesda, MD, USA). [35-36]. Regions of interest (ROI), each with a total area that encompassed a single bead, were selected for several beads and cytoplasmic (non-nuclear) cellular regions in each image. The mean of the measured ROI mean fluorescence intensities (FI) was calculated for beads and cellular regions in the image. The relative fluorescence intensity (RFI) of a given image was then calculated by normalizing cell mean FI by bead mean FI. All data are expressed as mean RFI (± SEM) for n = 7 - 10 cells. The SEM (standard error of the mean) represents the standard deviation of RFIs in cells exposed to the same treatment conditions. The statistical significance of the RFI difference between treated and untreated samples was assessed by the student's t-test.

Mean fluorescence intensity was related to CND average concentration by generating a standard curve from a confocal image series of CND solutions of known concentrations. Solutions of various CND concentrations were imaged in a layer above a coverslip on the confocal microscope with similar microscope setting usedfor cells loaded with CNDs. A single scan was performed at a depth well within the solution, and mean FI was measured in the center of the scanned field. A line was fit to the data and its slope determined. An image of calibration beads was also acquired using the same confocal microscope settings. The estimated equivalent CND concentration on a bead could then be calculated by dividing the bead mean FI and the slope of the standard curve (mean FI per uM). Using this method, calibration bead mean FI corresponded to an estimated 0.54 ± 0.18 μM CND. Intracellular concentration of CNDs for each sample was then estimated by assuming that an increase in RFI was related to a proportionate increase in CND concentration. The resulting RFI of each sample was converted to CND concentration by first subtracting the RFI of the control sample (to account for cell autofluorescence) and then multiplying the autofluorescence-corrected RFI by the estimated equivalent CND concentration of a calibration bead.

### TEM Imaging

The presence of silver nanoclusters in nanodevices enables the visualization of single particles (which appear as small grayish round objects) as well as aggregates (dark larger clusters) by TEM. Therefore, TEM was used to image CND localization inside treated cells.

### Ultrasonic Monitoring of Breakdown in Cells

Breakdown threshold for CNDs was defined as the lowest fluence that generated laser-induced bubbles acoustically detectable via a previously reported high-frequency technique [25,34]. Breakdown threshold is determined for each sample by monitoring bubble activity at variable average laser powers and evaluating maximum integrated backscatter (defined as the backscattered acoustic power from the bubble normalized to the power recorded for a perfect planar reflector using precisely the same transducer and electronics).

## RESULTS

### Silver CND Fabrication

Figure 2B shows an example of an SEC chromatogram (RI signal) of the targeted dendrimer template, PAMAM_E5.$(NH_2)_{42}(NGly)_{74}(NFA)_{2.7}$, which was used to determine molecular mass and polydispersity index. UV-vis spectra of FA (Figure 2B, inset A) and the identical UV-vis signal recorded at the maximum of elution peak (Figure 2B, inset B) indicates the successful substitution of FA molecules to PAMAM_E5.$(NH_2)_{45}(NGly)_{74}$, since they migrate together. A summary of analytical data is presented in Table 1. For details of experimental conditions and characterization see the supporting material. UV-vis data proved that conjugation of FA to PAMAM_E5.$(NH_2)_{45}(NGly)_{74}$ occurred at 2.7:1 molar ratio, in good agreement with synthesis conditions (see supporting material) and supported

by mass spectrometry. MALDI-TOF for PAMAM dendrimers can also be used to confirm these primary data, by comparing the change of molecular mass in the dominant peaks of consecutive synthesis products (assuming that individual molecules of the narrow distribution polymer were substituted with the same probability) [37-38]. For PAMAM derivatives, size exclusion chromatography multi-angle laser light scatter (SEC-MALLS) data usually cannot be used directly to calculate number of substituents based on mass differences, because loss of the lower molecular mass molecules during dialysis leads to an enrichment of the material in higher molecular mass components. For example, SEC mass difference suggests conjugation of 84 glycidol and 8 FA moieties, systematically more than NMR, UV-vis and MALDI-TOF data does.

CND particles are composed of 93% organic material (density ~1), and 7.03% of silver metal (density ~10.5), so the volume fraction of silver is around 0.7%. $\{(Ag^0)_{25}$-PAMAM_E5. $(NH_2)_{45}(NGly)_{74}\}$ i.e., non-targeted version of the silver/dendrimer composite ($\{Ag^0\}$ for short) was made from PAMAM_E5.$(NH_2)_{45}(NGly)_{74}$ templates. We have previously demonstrated that silver/dendrimer composite nanoparticles (without folate) are very stable; no precipitation was observed and the UV-vis profile did not change over one year in a closed vial [33]. The presence of 2.7 FA moieties (on average) per dendrimer template in the CNDs will not change its stability compared to $\{(Ag^0)_{25}$-PAMAM_E5.NGly}. Data indicate the formation of fluorescent nanoparticles with a diameter around 20 nm and a narrow size distribution (see supporting material). Fluorescence intensity of these silver composite nanoparticles is stable, and could thus be used as internal standards (see supporting material).

## Confocal Images of Cell Uptake of CNDs

Cells incubated with FA-$\{Ag^0\}$ solutions for twenty-four hours exhibited measurable concentration-dependent increases in intracellular fluorescence as compared to control cells (no CND incubation). A greater increase in cell fluorescence was observed for samples incubated with 0.5 μM CND solution than 0.050 μM CND solution. Figure 3 shows representative brightfield and color inverted fluorescence confocal microscopy images for five different cell treatment conditions (untreated, 0.5μM Untargeted CND treated, 0.5μM Targeted dendrimer template treated 0.05μM CND treated, and 0.5 μM CND treated). Confocal images of cells incubated with 0.05 μM CND solution mainly showed fluorescence in the cytoplasm, with relatively small fluorescence in the nucleus. In contrast, there was dramatic increase in both cytoplasmic and nuclear fluorescence of cells incubated with 0.5 μM CND solution.

RFI data for all conditions are summarized in Table 2. As Table 2 outlines, cells treated with 0.05μM and 0.5 μM targeted CNDs resulted in statistically significant increases in relative fluorescence intensity as compared to control cells (no CND incubation). Since the acquired confocal microscopic images of targeted CND-incubated cells are two-dimensional projections of three-dimensional fluorescence distribution over the 7.5μM optical slice thickness, increased RFI in these cells could result from both (or either) a uniform distribution of single CNDs or aggregates of CNDs. However, low RFI levels in cells treated with targeted dendrimer template (with no silver content) indicate minimal fluorescence (i.e., fluorescence originates from the silver CNDs) and those treated with untargeted silver CNDs suggests minimal nonspecific binding. As calculated, cells incubated with 0.05 μM and 0.5 μM CND solutions fluoresced with estimated intracellular CND concentrations of $0.13 \pm 0.22$ and $2.34 \pm 1.25$ μM respectively. According to these estimates, the average intracellular concentrations of CNDs were approximately 2-5 times higher than the concentration of the free unbound CNDs with which the cells were incubated (for detailed experimental conditions see supporting material). We emphasize that these data are good

estimates only, because (a) data were not integrated over multiple slices, and (b) the distribution of CNDs is inhomogeneous in the cell (see TEM images).

### TEM images of Cell Uptake of CNDs

Figures 4 display TEM images of KB cells incubated with the two targeted nanodevice concentrations (0.05 μM and 0.5 μM) and demonstrate differences in CND spatial distribution. For KB cells treated with 0.05 μM CNDs, Figure 4 A and B shows representative TEM images of single particles and small {Ag} agglomerates inside endosomal/lysosomal compartments of the cells. In contrast, Figure 4 C and D, which displays TEM images of cells treated with 0.5 μM CNDs, shows how single particles are distributed not only throughout the cell cytoplasm, but are present in the nucleus, as well in endosomal/lysosomal compartments. Some structures were engorged with the largest {Ag} clusters observed (see Figure 4 D). Similar to gold/dendrimer composite nanoparticles [39], internalization of the FA-CNDs have been mediated through receptor specific binding followed by endocytosis, which delivered the CNDs from the cell membrane into the cytoplasm where they were concentrated into larger clusters inside endosomal/lysosomal compartments (for experimental conditions see supporting material).

### Reduced Breakdown Threshold in Cells

Figure 5A displays time domain integrated bubble backscatter resulting from breakdown experiments in PBS, untargeted KB cells, and targeted cells incubated with 0.05 or 0.5 μM FA-{$Ag^0$} solution. Mean and standard deviation is displayed for fifty measurements. As Figure 5A shows, while KB cells incubated with 0.5 μM FA-{$Ag^0$} solution exhibited an order of magnitude threshold reduction, there was no threshold reduction in cells incubated with 0.05 μM folate-targeted solution. In addition, as Figure 5A shows, bubbles produced at reduced threshold powers have weaker backscatter, i.e., they are smaller than bubbles produced at higher powers.

Bubbles resulting from intracellular breakdown at reduced threshold powers also had shorter lifetimes than those produced at higher powers. This is shown in the acoustic wavefield plots of Figure 5B [27]. Bubble echoes were detected at the beginning of each laser exposure and persisted for the length of laser exposure (up to 1 second for these studies) at average powers above or near-threshold. For reduced powers, however, bubble echoes are detected at the beginning of laser exposure but sometimes persisted for only a few ultrasonic records. This transient behavior, while detected ultrasonically, limited the real-time optical observation of breakdown events at these reduced thresholds using the charge-coupled device (CCD) camera system described by Zohdy et al. (2005). Figure 6A summarizes bubble lifetimes obtained for CND-mediated intracellular breakdown. As laser power was decreased, bubble lifetime also decreased.

## DISCUSSION

Results demonstrated that a folate-targeted CND can be synthesized using a PAMAM_E5.$(NH_2)_{42}(NGly)_{74}(NFA)_{2.7}$ template. This FA-{$Ag^0$} was uptaken by KB cells in increased amounts compared to nontargeted CND. CND internalization caused a local reduction in NIR LIOB threshold for selective intracellular photodisruption of only labeled cells. CND-reduced-threshold breakdown required sufficiently high intracellular nanodevice concentrations to enhance the nonlinear optical absorption of the weakly absorbing cells.

Confocal images of CND treated cells showed increased relative fluorescence intensity compared to the negative control (untreated cells). It was estimated that cells incubated with 0.05 μM or 0.5 μM CND solution had intracellular CND concentrations of 0.13 ± 0.22 and

2.34 ± 1.25 μM respectively. The large standard deviations are likely due to both limitations in our estimation method and actual variations in local concentration resulting from heterogeneous intracellular distribution of CNDs. Nevertheless, these intracellular concentration estimates are within the ranges reported in previous studies, which investigated folate binding parameters and saturation kinetics for targeted dendrimers [40-41]. Intracellular concentration of internalized nanoparticles depends on the binding and internalization dynamics of folate-targeted particles and is affected by initial loading solution volumes and concentrations, as well as incubation times (all kept constant in this work).

Radioactive FA binding studies showed that KB cells bind ~1-10 μM of FA in the presence of extracellular concentrations of 0.005-0.1 μM of free FA [40]. Furthermore, other studies have shown that while the amount of folate-targeted dendrimers binding linearly increases at low loading concentrations, the concentration-response curve for binding quickly saturates. It has been reported in an example using KB cells that binding of folate-targeted dendrimers saturated at 0.57μM [41].

As expected, LIOB in targeted silver CND solution (2.5 μM in Phosphate buffered saline (PBS)) exhibited a 1.6 order of magnitude threshold reduction compared to water, greater than the one order of magnitude threshold reduction measured from the cells incubated with 0.5 μM untargeted $\{Ag^0\}$ CND solution. This suggests that the intracellular CND concentrations were probably less than 2.5 μM and the 2.34 ± 1.25 μM concentration predicted by the confocal fluorescence images of similarly prepared cells is reasonable. LIOB threshold studies on solutions with concentrations less than 2.5μM also did not exhibit the same threshold reduction as in concentration at or greater than 2.5μM. This is shown in Figure 6B, which shows bubble backscatter data and LIOB thresholds plotted for various CND concentrations. Different levels of laser energy (or fluence) provide bubble generation only around certain CND concentration levels. There probably exists a specific minimum CND concentration required for localized reduced-threshold LIOB to occur both in solution and intracellularly.

As is evidenced by their weaker backscatter and transient lifetimes, the size of the bubbles produced by CND-mediated reduced threshold LIOB are smaller, most likely much smaller than a KB cell diameter. Although absolute bubble size was not quantified from bubble backscatter data, we estimated a 3.2 to 6.2 μM diameter range (corresponding to a −65 to −60 dB backscatter range) from backscatter measurements from a range of polystyrene beads of known sizes [34].

The small size and transient behavior of the bubbles may limit real-time optical detection of this process. In previous intracellular breakdown studies by our group, the minimum fluence at which a visible microbubble (using an optical microscopy system described in Zohdy et al. (2005)), could be generated inside a cell with multiple pulses was more than twice the threshold of water. At reduced threshold, therefore, microbubbles could not be detected optically with the current system. Nevertheless, targeted CND-mediated laser-induced bubbles still provided an intracellular object for sensitive acoustic detection of targeted cells and potential manipulation.

The concentration dependence may be advantageous in preventing undesirable effects in untargeted cells from nonspecific binding of CNDs. Fluence level control can provide bubble generation only around concentrated CNDs and does not induce breakdown at low CND concentrations. We have shown experimentally that the effects of a laser-induced bubble are localized to the cell where the bubble is generated; surrounding cells are unaffected [20]. CND-mediated breakdown, therefore, provides a very precise, selective

mechanism for individual cell effects: no bubbles are generated in untargeted cells even it they accumulate some CNDs and for the cells that do accumulate enough intracellular CND concentration, laser-generated bubbles may be small enough to be nondestructive. Additionally, the use of longer excitation wavelengths (in the NIR) that have lower linear absorption has the potential to selectively affect targeted cells deep into tissue, generating enhanced nonlinear effects only in areas that accumulate the nanodevices.

The ability to create transient, acoustically detectable intracellular microbubbles with a targeted nanodevice breakdown procedure restricted to labeled cells has a number of potential applications in both biomedicine and basic biological research. For example, the potential precision of this technique would be especially useful in cases where the target cells are a very small portion among normal cells and must be either eliminated or identified (minimal residual disease for example in acute lymphoblastic leukemia) so that a new tumor does not develop. Relevant to more basic biologic studies, a CND-mediated photodisruption procedure could also enable highly localized, intracellular measurements utilizing the laser-generated bubbles as tools. For example, single bubbles have been investigated in recent studies as tools for acoustic radiation force imaging to measure elastic properties [42] and for acoustic activation to measure hydrostatic pressures in fluids [43]. For each application, bubbles must have lifetimes long enough for a useful effect or measurement.

## Supplementary Material

Refer to Web version on PubMed Central for supplementary material.

## Acknowledgments

This work was supported by the Whitaker Foundation, NIH grants EB-003449-01A1 and NOI-CO-27173, and NCI Cancer Support Grant CA016056 to the Roswell Park Cancer Institute. The NIH Resource Center for Medical Ultrasonic Transducer Technology at USC supplied high frequency transducers, IntraLase Corporation supplied the ultrafast laser, the Microscopy & Image Analysis Laboratory at the University of Michigan helped with the confocal microscopy and TEM work.

## REFERENCES

1. Hirsch LR, Stafford RJ, Sershen SR, Halas NJ, Hazle JD, West JL. Nanoshell-assisted tumor ablation using near infrared light under magnetic resonance guidance. Proc. Natl. Acad. Sci. USA 2003;100:113549–54.
2. Pitsillides CM, Joe EK, Wei X, Anderson RR, Lin CP. Selective cell targeting with light-absorbing microparticles and nanoparticles. Biophys. J 2003;84:4023–4032. [PubMed: 12770906]
3. O'Neal DP, Hirsch LR, Halas NJ, Payne JD, West JL. Photo-thermal tumor ablation in mice using near infrared-absorbing nanoparticles. Cancer Lett 2004;209:171–176. [PubMed: 15159019]
4. Zharov VP, Letfullin RR, Galitovskaya EN. Microbubbles-overlapping mode for laser killing of cancer cells with absorbing nanoparticle clusters. J. Phys. D: Appl. Phys 2005;38:2571–2581.
5. Zharov VP, Kim JW, Everts M, Curiel DT. Self-assembling nanoclusters in living systems: application for integrated photothermal nanodiagnostics and nanotherapy (review). J. Nanomed 2005;1:326–345.
6. Loo C, Lowery A, Halas N, West J, Drezek R. Immunotargeted Nanoshells for Integrated Cancer Imaging and Therapy. NanoLetters 2005;5:709–11.
7. Zharov VP, Galitovskaya EN, Jonson C, Kelly T. Synergistic enhancement of selective nanophotothermolysis with gold nanoclusters: potential for cancer therapy. Laser Surg Med 2005;37:219–226.
8. El-Sayed IH, Huang X, El-Sayed MA. Selective laser photo-thermal therapy of epithelial carcinoma using anti-EGFR antibody conjugated gold nanoparticles. Cancer Letters 2006;239(1):129–135. [PubMed: 16198049]

9. Pissuwan D, Valenzuela SM, Cortie MB. Therapeutic possibilities of plasmonically heated gold nanoparticles. Trends in Biotechnol 2006;24(2):62–67.
10. Huang X, Jain PK, El-Sayed IH, El-Sayed MA. Determination of the Minimum Temperature Required for Selective Photothermal Destruction of Cancer Cells with the Use of Immunotargeted Gold Nanoparticles. Photochemistry and Photobiology 2006;82(2):412–417. [PubMed: 16613493]
11. Huang X, El-Sayed IH, Qian W, El-Sayed MA. Cancer Cell Imaging and Photothermal Therapy in the Near-Infrared Region by Using Gold Nanorods. J. Am. Chem. Soc 2006;128(6):2115–2120. [PubMed: 16464114]
12. Everts M, Saini V, Leddon JL, Kok RJ, Stoff-Khalili M, Preuss MA, et al. Covalently linked Au nanoparticles to a viral vector: potential for combined photothermal and gene cancer therapy. Nano. Lett 2006;6(4):587–591. [PubMed: 16608249]
13. Khlebtsov B, Zharov V, Melnikov A, Tuchin V, Khlebtsov N. Optical amplification of photothermal therapy with gold nanoparticles and nanoclusters. Nanotechnology 2006;17:5167–5179.
14. Lapotko D, Lukianova E, Potapnev M, Aleinikova O, Oraevsky A. Method of laser activated nano-thermolysis for elimination of tumor cells. Cancer Lett 2006;239(1):36–45. [PubMed: 16202512]
15. Vogel A, Venugopalan V. Mechanisms of Pulsed Laser Ablation of Biological Tissues. Chem. Rev 2003;103:577–644. [PubMed: 12580643]
16. König K, Riemann I, Fischer P, Halbhuber KJ. Intracellular nanosurgery with near infrared femtosecond laser pulses. Cell. Mol. Biol 1999;45(2):195–201. [PubMed: 10230728]
17. König K, Riemann I, Fritzsche W. Nanodissection of human chromosomes with near-infrared femtosecond laser pulses. Optics Letters 2001;26(11):819–821. [PubMed: 18040461]
18. Tirlapur UK, König K. Targeted transfection by femtosecond laser light. Nature 2002;418:290–291. [PubMed: 12124612]
19. Yanik MF, Cinar H, Cinar HN, Chisholm AD, Jin Y, Ben-Yakar A. Functional regeneration after laser axotomy. Nature 2004;432(7019):822. [PubMed: 15602545]
20. Zohdy MJ, Tse C, Ye JY, O'Donnell M. Optical and acoustic detection of laser-generated microbubbles in single cells. IEEE Trans. on UFFC 2005;53(1):117–125.
21. Balogh L, Swanson DR, Spindler R, Tomalia DA. Formation and Characterization of Dendrimer-Based Water Soluble Inorganic Nanocomposites. Proceedings of American Chemical Society Polymeric Materials Science and Engineering 1997;77:118–119.
22. Balogh L, Valluzzi R, Laverdure KS, Gido SP, Hagnauer GL, Tomalia DA. Formation of Silver and Gold Dendrimer Nanocomposites. J. Nanopart. Res 1999;1(3):353–368.
23. Balogh L, Laverdure KS, Gido SP, Mott AG, Miller MJ, Ketchel BP, et al. Dendrimer-Metal Nanocomposites. In: Organic/Inorganic Hybrid Materials. Mat. Res. Soc. Symp. Proc 1999;576:69–75.
24. Ye JY, Balogh L, Norris TB. Enhancement of Laser-Induced Breakdown Using Metal/Dendrimer Nanocomposites. Appl. Phys. Lett 2002;80:1713–1715.
25. Milas SM, Ye JY, Norris TB, Balogh LP, Baker JR Jr, Hollman KW, et al. Acoustic Characterization of Enhanced Laser-Induced Optical Breakdown Using Silver/Dendrimer Nanocomposites. Appl. Phys. Lett 2003;82:994–996.
26. Tomalia, DA.; Dvornic, P. Dendritic Polymers, Divergent Synthesis (Starburst Polyamidoamine Dendrimers). In: Salamone, JC., editor. Polymeric Materials Encyclopedia. Vol. 3. CRC Press; New York: 1996. p. 1814-1830.
27. Patri AK, Majoros IJ, Baker JR Jr. Dendritic polymer macromolecular carriers for drug delivery. Current Opinion in Chemical Biology 2002;6:466–471. [PubMed: 12133722]
28. Patri AK, Thomas T, Baker JR Jr. Bander NH. Antibody-Dendrimer Conjugates for Targeted Prostate Cancer Therapy. Polymeric Materials: Science & Engineering 2002;86:130.
29. Shukla R, Thomas TP, Peters J, Kotlyar A, Myc A, Baker JR Jr. Tumor angiogenic vasculature targeting with PAMAM dendrimer-RGD conjugates. Chem. Commun 2005;46:5739–5741.
30. Lesniak WG, Kariapper MST, Nair BM, Balogh LP, Khan MK. Synthesis and Characterization of PAMAM Dendrimer Based Multifunctional Nanodevices for Targeting $a_V b_3$ Integrins. Bioconjugate Chemistry 2007;18:1148–1154. [PubMed: 17566976]

31. Wiener EC, Konda S, Shadron A, Brechbiel M, Gansow O. Targeting dendrimer-chelates to tumors and tumor cells expressing the high-affinity folate receptor. Invest. Radiol 1997;32(12): 748–754. [PubMed: 9406015]
32. Quintana A, Raczka E, Piehler L, Lee I, Myc A, Majoros I, et al. “Design and Function of a Dendrimer-Based Therapeutic Nanodevice Targeted to Tumor Cells Through the Folate Receptor. Pharmaceutical Research 2002;19:1310–1316. [PubMed: 12403067]
33. Lesniak W, Bielinska AU, Sun K, Janczak KW, Shi X, Baker JR Jr. et al. Silver/Dendrimer Nanocomposites as Biomarkers: Fabrication, Characterization, in Vitro Toxicity, and Intracellular Detection. Nano 2005;5(11):2123–2130.
34. Tse C, Zohdy MJ, Ye JY, Norris TB, Balogh L, Hollman K, et al. Acoustic Detection of Controlled Laser-Induced Microbubble Creation in Gelatin. IEEE Transactions on Ultrasonics, Ferroelectrics, and Frequency Control 2005;52(11):1962–1969.
35. Rasband, WS. ImageJ. U. S. National Institutes of Health; Bethesda, Maryland, USA: 1997-2007. http://rsb.info.nih.gov/ij/
36. Abramoff MD, Magelhaes PJ, Ram SJ. Image Processing with ImageJ. Biophotonics International 2004;11(7):36–42.
37. Zhang C, O'Brien S, Balogh L. Comparison and Stability of CdSe Nanocrystals Covered with Amphiphilic Poly(Amidoamine) Dendrimers. J. Phys. Chem. B 2002;106(40):10316–10321.
38. Shi X, Bányai I, Islam MT, Lesniak W, Davis DZ, Baker JR Jr. et al. Generational, skeletal and substitutional diversities in generation one poly(amidoamine) dendrimer. Polymer 2005;46(9): 3022–3034.
39. Bielinska A, Eichman JD, Lee I, Baker JR Jr. Balogh LP. Imaging {$Au^0$-PAMAM} Gold-Dendrimer Nanocomposites In Cells. J. of Nanoparticle Research 2002;4:395–403.
40. Thomas TP, Myaing MT, Ye JY, Candido K, Kotlyar A, Beals J, et al. Detection and Analysis of Tumor Fluorescence Using a Two-Photon Optical Fiber Probe. Biophysical Journal 2004;86:3959–3965. [PubMed: 15189892]
41. Ye JY, Myaing MT, Norris TB. Biosensing based on two-photon fluorescence measurements through optical fibers. Optics Letters 2002;27(16):1412–1414. [PubMed: 18026463]
42. Erpelding TN, Hollman KW, O'Donnell M. Bubble-based acoustic radiation force elasticity imaging. IEEE Trans. Ultrason. Ferroelect. Freq. Control 2005;52(6):971–979.
43. Postema M, Bouakaz A, de Jong N. Noninvasive microbubble-based pressure measurements: A simulation study. Ultrasonics 2004;42:759–762. [PubMed: 15047379]

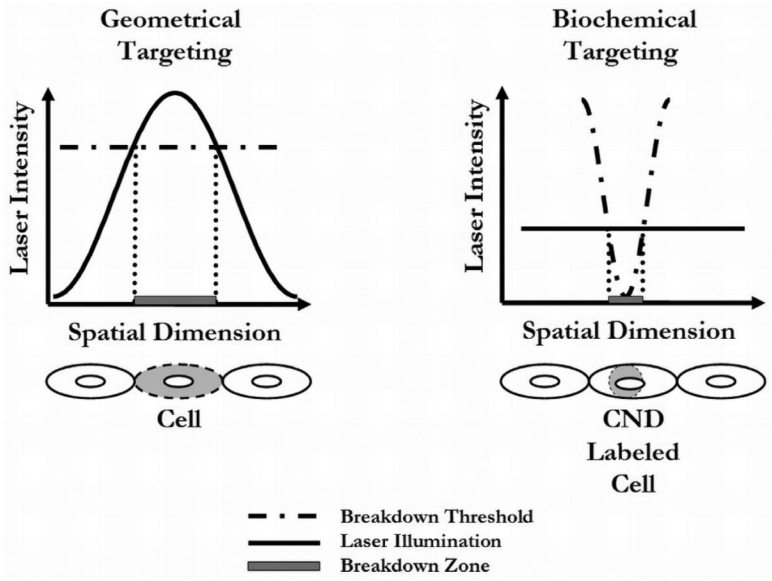


**Figure 1.**
Schematic of geometrically and biochemically targeted breakdown. In geometrically targeted breakdown, the local laser intensity variation achieved by focusing defines the breakdown region. In biochemically targeted breakdown, the spatial distribution of the molecular nanosystem (and thus breakdown threshold variation) defines the breakdown region.

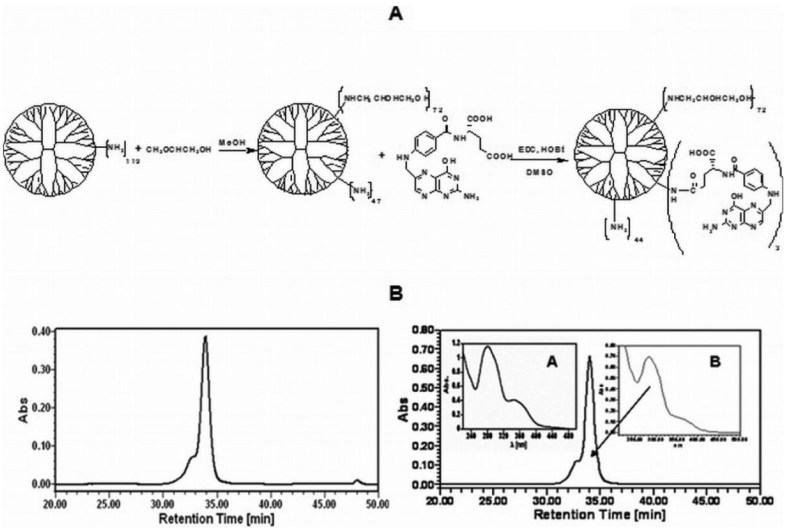


**Figure 2.**

A. Scheme: Synthesis of FA conjugated PAMAM dendrimer nanodevice terminated with primary amine and glycidol groups. Subscripts denote actual numbers of the average functionalities measured by various analytical methods. B. SEC Analysis (UV signal at 250nm) of PAMAM_E5.$(NH_2)_{45}(NGly)_{74}$ (left panel) and PAMAM_E5. $(NH_2)_{42}(NGly)_{74}(NFA)_{2.7}$ (right panel); Insert A: UV-vis spectrum of folic acid; Insert B: UV-vis spectrum at 34 min of the elution signal.

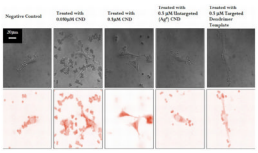

**Figure 3.**
Representative confocal brightfield (top) and color inverted fluorescent (bottom) images for various treatment conditions. From left to right: control KB cells (no CND incubation), KB cells incubated with 0.05 μM FA-{$Ag^0$} folate targeted CND, KB cells incubated with 0.5 μM folate targeted FA-{$Ag^0$}, KB Cells incubated with 0.5 μM untargeted {$Ag^0$} CND, and KB Cells incubated with 0.5 μM targeted dendrimer template. Spherical objects in all three images are CND-covered beads used as internal standard. Scale bar, 20μM.

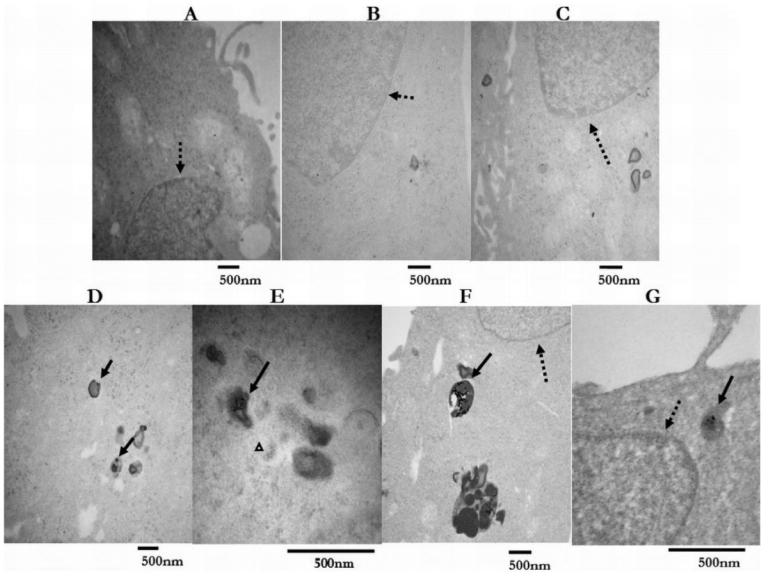


**Figure 4.**

A,B,and C. Representative TEM images of control KB cells (no CND incubation), KB cells treated with 0.5 μM targeted dendrimer template, and KB cells treated with 0.5 μM untargeted $\{Ag^0\}$ CND. D and E. Representative TEM images of KB cells treated with 0.05 μM CND. Complex aggregates (solid arrows) visible inside endosomal/lysosomal compartments. Very few single particles (small grayish round objects) observed in cytoplasm (white triangular pointer). F and G. Representative TEM images of KB cells treated with 0.5 μM FA-$\{Ag^0\}$. Large complex aggregates (solid arrows) visible inside endosomal/lysosomal compartments. Single particles (small grayish round objects) randomly distributed and visible in cytoplasm and nuclear regions (dashed arrow).

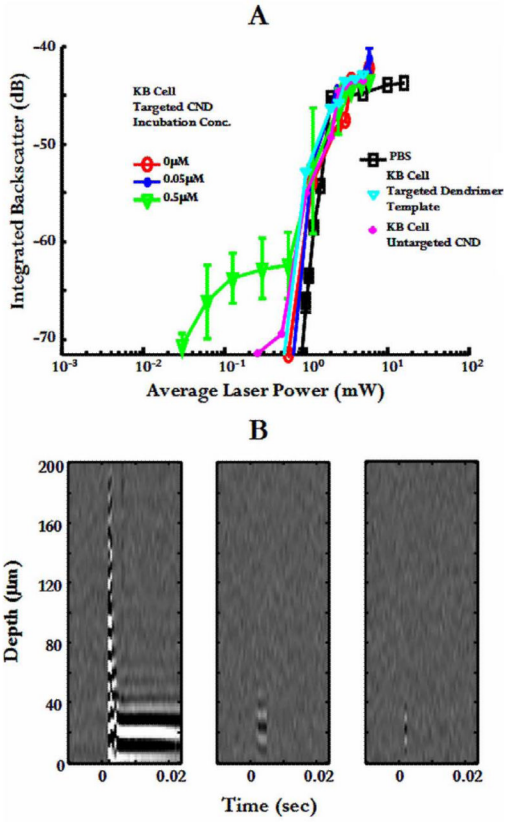


**Figure 5.**

A. Maximum integrated backscatter from laser-induced bubbles in treated cell monolayers vs. average laser power. B. Wavefield plots of intracellular breakdown at 3 different average laser powers: 1.2 mW, 0.6 mW, and 0.12 mW.

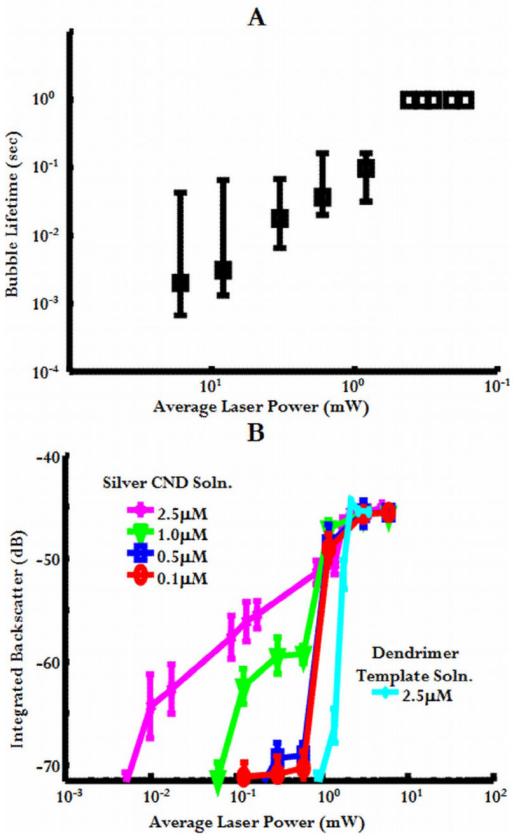


**Figure 6.**

A. Maximum, median, and minimum lifetimes of bubbles produced from breakdown in KB cells treated with 0.5 μM CND solution. Data points without error bars indicate that bubbles lasted the entire experimentation interval (bubble lifetimes were longer than the monitoring time). B. Maximum integrated backscatter from laser-induced bubbles in targeted CND solution concentrations of and less than 2.5 μM.

**Table 1**

Characterization of Dendrimer Templates

| # | terminal groups | no. of groups measured by potentiometry | Molecular mass measured by SEC | no. of groups measured by UV-vis | mass indicated by MALDI | no. of groups measured by NMR |
|---|---|---|---|---|---|---|
| 1 | -$NH_2$ | **119** | Mn 27280<br>Mw 30280<br>Mw/Mn 1.010 | ---- | 26572 | ---- |
| 2 | -NGly | ---- | Mn 32180<br>Mw 35890<br>Mw/Mn 1.115 | --- | 32292<br># of Gly: 76 | **74** |
| 3 | -NH-FA | ---- | Mn 35660<br>Mw 40820<br>Mw/Mn 1.119 | **# of FA: 2.7** | 34210<br>#of FA: 4.3 | N/A |

1 - PAMAM_E5.$(NH_2)_{119}$ (starting material); 2 - PAMAM_E5.$(NH_2)_{45}(NGly)_{74}$ (intermediate); 3 - PAMAM_E5.$(NH_2)_{42}(NGly)_{74}(NFA)_{2.7}$ (template that is partially glycidolated and conjugated with folic acid). Average numbers of substituents (in bold) were calculated from the most precise methods for the given substituents, i.e., potentiometric titration for primary amines, NMR for the $NHCH_2CH(OH)CH_2OH$ (Gly) termini and UV-vis spectroscopy for folic acid. Accuracy of data is estimated as ±5%. In MALDI spectra, the highest frequency fragment in the major peaks was considered as center of molecular mass, because their values shift according to the consecutive modifications [33].

## Table 2

Confocal Imaging of KB Cell Uptake of CNDs

| | Treatment Condition | Relative Fluorescence Intensity (RFI, mean ± SEM) | Estimated CND concentration (μM) |
|---|---|---|---|
| 1 | Negative Control | 0.85 ± 0.26 | - |
| 2 | 0.05 μM Targeted CNDs | 1.1 ± 0.29* | 0.13 ± 0.22 μM |
| 3 | 0.5 μM Targeted CNDs | 5.2 ± 1.8* | 2.34 ± 1.25 μM |
| 4 | 0.5 μM Untargeted {$Ag^0$} CND | 0.87 ± 0.24 | - |
| 5 | 0.5 μM Targeted Dendrimer Template | 0.86 ± 0.18 | - |

*statistically significant difference compared to negative control ($p<0.01$). 1) a negative control (no CND incubation), 2) incubation with 0.05 μM targeted CND {$(Ag^0)_{25}$ - PAMAM_E5. $(NH_2)_{42}(NGly)_{74}(NFA)_{2.7}$} solution, 3) incubation with 0.5 μM targeted CND {$(Ag^0)_{25}$ - PAMAM_E5.$(NH_2)_{42}(NGly)_{74}(NFA)_{2.7}$} solution, 4) incubation with 0.5 μM untargeted CND {$(Ag^0)_{25}$-PAMAM_E5.$(NH_2)_{45}(NGly)_{74}$} solution and 5) incubation with 0.5 μM targeted dendrimer template {PAMAM_E5.$(NH_2)_{42}(NGly)_{74}(NFA)_{2.7}$} (no silver).